# Chapter 10
# Mechano-Chemical Fluid-structure Interactions and Active Materials

Many aspects in solid dynamics cannot be explained by an elastic response of the material. In some applications, the material undergoes active changes, e.g. by growth, swelling or generation of material, by chemically induced contractions or bending. In other situations, the reference state is not stress-free. If a log of wood is cut in two pieces, these will afterwards deform and spread.

One model for the realization of active material modification is the introduction of an intermediate material configuration, the *grown configuration*, that is assumed to include the active growth or change of material, a configuration that is stress-free but non-physical, see Rodriguez et al. [291] and Jones and Chapman [209] for further examples. We call this configuration $\hat{S}_a$, the active one and introduce a mapping that describes only this growth process

$$\hat{T}_a(t) : \hat{S} \to \hat{S}_a(t)$$

and that maps the Lagrangian reference state to the grown one. In Fig. 10.1 we show two possible models for active material growth, isotropic growth of control volumes and a volume-conserving constriction of control volumes. The grown state is understood to be stress-free but non-physical, as control volumes might overlap.

In a second step, the solid elastically reacts to this intermediate configuration. We denote by

$$\hat{T}_e(t) : \hat{S}_a(t) \to S(t)$$

the mapping of this elastic response. The overall material deformation is given by

$$\hat{T}(t) : \hat{S} \to S(t), \quad \hat{T}(t) = \hat{T}_e(t) \circ \hat{T}_a(t). \tag{10.1}$$
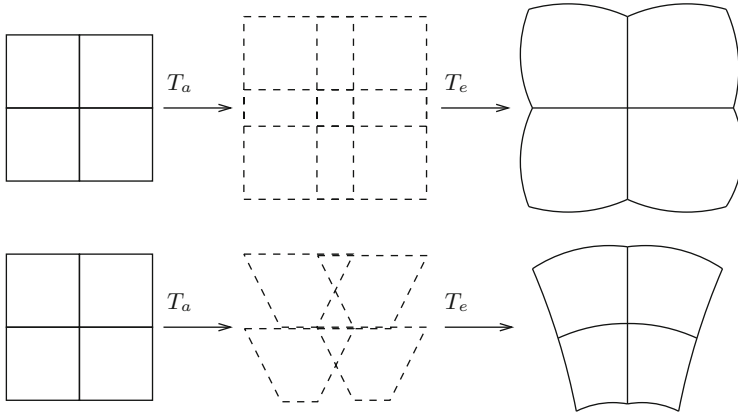
**Fig. 10.1** Two different kinds of active material deformation. *Top row*: isotropic growth. *Bottom*: Constriction of volume elements. The intermediate configuration is grown and stress-free but not physical

The complete deformation $\hat{\mathcal{S}} \to \hat{\mathcal{S}}(t)$ is still described by $\hat{\mathbf{u}}$ including growth and elasticity, such that

$$\hat{T}(\hat{x}, t) = \hat{x} + \hat{\mathbf{u}}(\hat{x}, t).$$

As usual, we introduce the deformation gradient and its determinant

$$\hat{\mathbf{F}} := \hat{\nabla}\hat{T}, \quad \hat{J} := \det \hat{\mathbf{F}}. \tag{10.2}$$

The splitting into growth and elastic response is done on the level of the deformation gradient, see Fig. 10.2. We introduce

$$\hat{\mathbf{F}}_a := \hat{\nabla}\hat{T}_a, \quad \hat{J}_a := \det \hat{\mathbf{F}}_a, \tag{10.3}$$

and

$$\hat{\mathbf{F}}_e := \hat{\nabla}\hat{T}_e, \quad \hat{J}_e := \det \hat{\mathbf{F}}_e, \tag{10.4}$$

By means of (10.1) it holds

$$\hat{\mathbf{F}} = \hat{\mathbf{F}}_e\hat{\mathbf{F}}_a, \quad \hat{J} = \hat{J}_e\hat{J}_a.$$
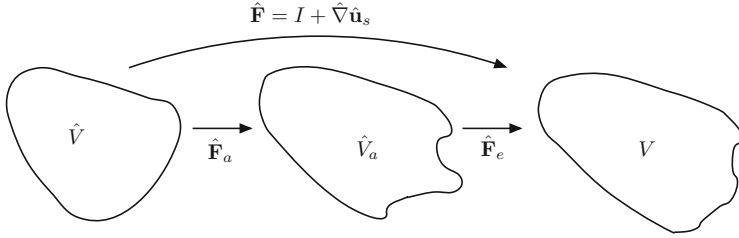
**Fig. 10.2** Multiplicative decomposition of the deformation gradient into active part $\mathbf{F}_a$ and elastic response $\mathbf{F}_e$

If we assume that $\hat{T}_a$ is given by an external mechanism we can compute the elastic deformation gradient based on the deformation $\mathbf{u}$ and this growing part

$$\hat{\mathbf{F}}_e = \hat{\mathbf{F}}\hat{\mathbf{F}}_a^{-1} = (I + \hat{\nabla}\hat{\mathbf{u}})\hat{\mathbf{F}}_a^{-1}.$$

Now, stresses will depend solely on this elastic part. In terms of Definition 2.18, the first Piola Kirchhoff stress tensor of the St. Venant Kirchhoff material is given by

$$\hat{\mathbf{P}}_e = \hat{\mathbf{F}}_e\hat{\mathbf{\Sigma}}_e = 2\mu_s\hat{\mathbf{F}}_e\hat{\mathbf{E}}_e + \lambda_s\,\mathrm{tr}(\hat{\mathbf{E}}_e)\hat{\mathbf{F}}_e, \quad \hat{\mathbf{E}}_e := \frac{1}{2}(\hat{\mathbf{F}}_e^T\hat{\mathbf{F}}_e^T - I). \tag{10.5}$$

The tensor $\hat{\mathbf{P}}_e$ is formulated on the intermediate configuration $\hat{\mathcal{S}}_a(t)$. The equations of conservation are however given on the non-strained, non-grown reference configuration $\hat{\mathcal{S}}$. Therefore, in a last step we must pull back this tensor to $\hat{\mathcal{S}}$. We refer to [73]

$$\hat{\mathbf{\Sigma}} = \hat{J}_a\hat{\mathbf{F}}_a^{-1}\hat{\mathbf{\Sigma}}_e\hat{\mathbf{F}}_a^{-T}. \tag{10.6}$$

## 10.1   Growth Models

*Growth* can come in various forms. It is possible that new material is added. Then, material can simply swell while conserving its mass. *Growth* can also be the change of configuration without change of volume or mass, e.g. shearing or rotation.

We first consider the case, where the same type of material is locally added in an isotropic fashion. Let $\hat{V}$ be a control volume and $\hat{x}_0 \in \hat{V}$ be a reference point. We assume that this control volume isotropically growing

$$\hat{V} \to V_a(t), \quad V_a(t) := \{\hat{x}_0 + \alpha t(\hat{x} - \hat{x}_0),\ \hat{x} \in \hat{V}\},$$

where by $\alpha \in \mathbb{R}$ we denote the *growth rate*, see Fig. 10.1. By

$$\hat{T}_a(\hat{x}, t) = \hat{x} + \alpha t(\hat{x} - \hat{x}_0), \quad \hat{\mathbf{F}}_a = \hat{\nabla}\hat{T}_a = (1 + \alpha t)I, \quad \hat{J}_a = (1 + \alpha t)^d \quad (10.7)$$

we can express the active mapping and deformation gradient, where $d > 0$ is the spatial dimension. We assume that the new material has the same density $\hat{\rho}^0$, such that mass is added (or decreased for $\alpha < 0$)

$$m(V_a(t)) = \int_{V_a(t)} \rho^0 \, dx = \int_{\hat{V}} \hat{J}_a \rho^0 \, d\hat{x} =: \int_{\hat{V}} \hat{\rho}_a \, d\hat{x}.$$

By

$$\hat{\rho}_a := \hat{J}_a \hat{\rho}^0 = (1 + \alpha t)^d \hat{\rho}^0, \tag{10.8}$$

we denote the grown density in the reference configuration.

Second, we consider the swelling of material, an isotropic growth without addition or removal of mass. The growth map is given as in (10.1), the mass however is conserved from $\hat{V}$ to $V_a(t)$

$$m(\hat{V}) = \int_{\hat{V}} \hat{\rho}^0 \, d\hat{x} \overset{!}{=} \int_{V_a(t)} \rho_a \, dx = \int_{\hat{V}} \hat{J}_a \hat{\rho}_a \, d\hat{x} = \int_{\hat{V}} (1 + \alpha t)^d \hat{\rho}_a \, d\hat{x},$$

such that

$$\hat{\rho}_a = (1 + \alpha t)^{-d} \hat{\rho}^0.$$

Third, we consider the case of a constriction, where both mass and volume of the control volumes stays the same, see the bottom row of Fig. 10.1. Let $\hat{V}$ be a reference volume and $\hat{x}^0 \in V$ be its center of mass. In two spatial dimensions, the active map is given by

$$\hat{T}_a(\hat{x}, t) = \begin{pmatrix} \hat{x}_1^0 + (\hat{x}_1 - \hat{x}_0^1)(1 + \alpha t(\hat{x}_2 - \hat{x}_2^0)) \\ \hat{x}_2 \end{pmatrix},$$

with deformation gradient and determinant

$$\hat{\mathbf{F}}_a(\hat{x}, t) = \begin{pmatrix} 1 + \alpha t(\hat{x}_2 - \hat{x}_2^0) & (\hat{x}_1 - \hat{x}_1^0)\alpha t \\ 0 & 1 \end{pmatrix}, \quad \hat{J}_a = 1 + \alpha t(\hat{x}_2 - \hat{x}_2^0).$$

## 10.2   Model Case: Formation and Growth of Atherosclerotic Plaques

We consider the coupled dynamics of an incompressible fluid with an elastic structure that undergoes active growth and deformation by bio/chemical processes. The mechanical fluid-structure interaction problem is coupled to the dynamics of chemical species that are transported that react and diffuse and that finally will cause solid growth. This model is a generalization of a detailed model for the dynamics of the formation and growth of plaques in blood vessels that has been discussed in [354–356].

We introduce a simplified model that describes the formation and growth of plaques in large blood vessels. For simplicity, we denote by $\Omega(t) \subset \mathbb{R}^2$ a two-dimensional domain, split into the vessel wall $\mathcal{S}(t) \subset \mathbb{R}^2$ and the fluid domain $\mathcal{F}(t) \subset \mathbb{R}^2$, which is occupied by blood. The interface between fluid and solid is denoted by $\mathcal{I}(t)$, see Fig. 10.3. We model blood as an incompressible Newtonian and homogenous fluid. The vessel wall is described by the St. Venant Kirchhoff material as stated above.

Our model for the fluid-solid interaction problem between blood and the vessel is overly simplified. The mechanical properties of vessels are complex with multi-layered anisotropic structures. We refer to the literature for advanced models and also for numerical approaches to deal with them [87, 147, 149, 195].

In short, the biological mechanism is evolving as follows (compare Fig. 10.3): First, monocytes (concentration called $c_f$) are transported by an advection-diffusion process within the blood flow. Second, they penetrate damaged parts of the vessel wall (in damaged areas) where they are transformed to macrophages (called $c_s$). The migration rate depends on the difference of monocyte and macrophage concentration ($c_f - c_s$) on the interface, on the wall stress and the damage condition of the wall. Thirdly, within the vessel wall, the macrophages are again transported by an advection-diffusion process and transformed into foam cells (called $c_s^*$). Finally, accumulation of foam cells leads to plaque growth.

This problem is coupled to the dynamics of the fluid-structure interaction problem. Due to hemodynamical forces driven by the pulsating flow, the geometry deforms substantially. Furthermore, the formation of plaques significantly changes
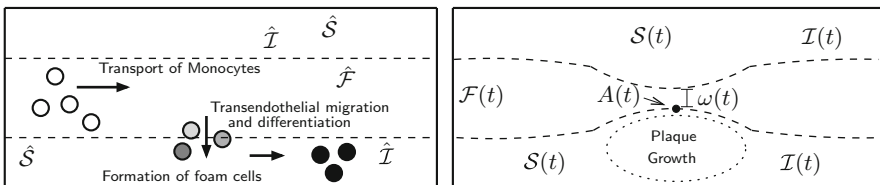


**Fig. 10.3** Configuration of the domain and mechanism of plaque formation. *Left*: Domain in reference configuration split into fluid part $\hat{\mathcal{F}}$ and solid $\hat{\mathcal{S}}$ divided by the interface $\hat{\mathcal{I}}$. *Right*: Domain in the current (Eulerian) description with plaque formation and narrowing of vessel

the domains. Finally, the hemodynamical forces influence the penetration of monocytes into the vessel wall and therefore a two-way coupled problem must be considered. The complete set of equations is given by

$$
\left.\begin{aligned}
\rho_f(\partial_t \mathbf{v}_f + \mathbf{v}_f \cdot \nabla \mathbf{v}_f) - \operatorname{div} \boldsymbol{\sigma}_f &= 0 \\
\operatorname{div} \mathbf{v}_f &= 0 \\
\partial_t c_f + \mathbf{v}_f \cdot \nabla c_f - D_f \Delta c_f &= 0
\end{aligned}\right\} \text{ in } \mathcal{F}(t)
$$

$$
\left.\begin{aligned}
\rho_s(\partial_t \mathbf{v}_s + \mathbf{v}_s \cdot \nabla \mathbf{v}_s) - \operatorname{div} \boldsymbol{\sigma}_s &= 0 \\
\partial_t c_s + \mathbf{v}_s \cdot \nabla c_s - D_s \Delta c_s &= -\beta c_s \\
\partial_t c_s^* + \mathbf{v}_s \cdot \nabla c_s^* &= \beta c_s
\end{aligned}\right\} \text{ in } \mathcal{S}(t) \qquad (10.9)
$$

$$
\left.\begin{aligned}
\boldsymbol{\sigma}_f \mathbf{n}_f + \boldsymbol{\sigma}_s \mathbf{n}_s &= 0 \\
\mathbf{v}_f &= \mathbf{v}_s \\
D_f \nabla c_f \mathbf{n}_f + D_s \nabla c_s \mathbf{n}_s &= 0 \\
D_s \nabla c_s \mathbf{n}_s &= \zeta(c_f - c_s)
\end{aligned}\right\} \text{ on } \mathcal{I}(t)
$$

Here, $\mathbf{v}_f$ and $\mathbf{v}_s$ stand for the fluid and solid velocity. By $\rho_f$ and $\rho_s$ we denote the densities of blood and vessel wall and by $\mathbf{n}_f$ and $\mathbf{n}_s$ the outer normals of the fluid and solid domain, respectively. $D_f$ and $D_s$ are diffusion coefficients for monocytes and macrophages. In particular $D_s$ depends on the concentration of foam cells $c_s^*$ [355]. The coefficient $\zeta$ describes the migration of monocytes through the vessel wall. This parameter will depend on the hemodynamical stress $\zeta = \zeta(\boldsymbol{\sigma}_f \mathbf{n})$. The parameter $\beta$, usually depending on the concentration of foam cells, controls the transformation of macrophages to foam cells.

One of the major challenges in plaque modeling is the huge variety of temporal scales: While the heart beats once in about every 1 s, plaque growth takes place in a time span of months, i.e. $T \gg 1{,}000{,}000$ s. Although all scales have a significant influence on the coupled dynamics, a numerical simulation will not be able to resolve each detail while following the long-term process. Instead, we—as most approaches—consider an averaged flow problem and focus on the long-scale dynamics. Effective model parameters controlling the migration of monocytes through the vessel walls will be obtained by local (in time) small-scale simulations. The analysis of temporal multiscale problems with partial differential equations is still an open problem. Also we do not know efficient numerical multiscale methods for the approximation of such problems. We refer to the forthcoming dissertation of Sonner [315] for first steps in this direction.

Rather than developing a quantitative model, we concentrate in this paper on a robust numerical framework for the coupled long-term dynamics of fluid-structure interaction with active growth processes and large deformation. Hence, the approximation of the chemical dynamics plays a minor role. We therefore strongly simplify Model (10.9) and replace the complete chemical dynamics by a simple ode

modeling the total concentration of foam cells

$$\partial_t c_s^*(t) = \gamma(\boldsymbol{\sigma}_{WS}, t), \quad c_s^*(0) = 0, \tag{10.10}$$

where the function $\gamma$ specifies the rate of foam cell accumulation. Here, this function depends on the wall stress in main stream direction $\boldsymbol{\sigma}_{WS}$

$$\gamma(\boldsymbol{\sigma}_{WS}, t) = \gamma_0 \left(1 + \frac{\boldsymbol{\sigma}_{WS}(t)}{\overline{\sigma}}\right)^{-1}, \quad \overline{\sigma} = 50 \frac{\mathrm{g}}{\mathrm{cm} \cdot \mathrm{s}^2}, \quad \gamma_0 = 5 \cdot 10^{-7}. \tag{10.11}$$

For details on models of the dependency of the monocyte migration rate on the wall stress we refer to [78]. The exact role and influence of the wall stress on the migration rate is not yet completely understood. For further discussion, we refer to [99]. The scalar concentration $c_s^* : [0, T] \rightarrow \mathbb{R}_+$ will directly determine the active growth. Growth will take part in the middle parts of the vessel walls, see Fig. 10.3.

Accurate handling of the different time-scales is an open problem. Most approaches use an averaging in time and focus on the long-scale dynamics only [94, 355]. A two-scale approach has been suggested in [158]. Here, we simply consider an averaged long-scale model. We neglect the pulsating flow and instead choose one constant inflow-rate. We fully acknowledge that this approach will result in enormous modeling errors and refer to [158] for a detailed discussion.

**Problem 10.1 (Long-Scale Growth)**   *In $I = [0, T]$, find fluid-velocity $\mathbf{v}_f$, pressure $p_f$, solid deformation $\mathbf{u}_s$ and foam cell concentration $c_s^*$, given by*

$$\begin{aligned}
\rho_f \mathbf{v}_f \cdot \nabla \mathbf{v}_f - \mathrm{div}\,\boldsymbol{\sigma}_f = 0, \quad \mathrm{div}\,\mathbf{v}_f = 0 \quad & in\ \mathcal{F}(t) \\
- \mathrm{div}\,\boldsymbol{\sigma}_s(c_s^*(t)) = 0 \quad & in\ \mathcal{S}(t) \\
\mathbf{v}_f = 0, \quad \boldsymbol{\sigma}_f \mathbf{n}_f + \boldsymbol{\sigma}_s(c_s^*(t))\mathbf{n}_s = 0 \quad & on\ \mathcal{I}(t) \\
\partial_t c_s^*(t) = \gamma(\boldsymbol{\sigma}_{WS}), \quad c_s^*(0) = 0 \quad & in\ \mathcal{S}(t).
\end{aligned} \tag{10.12}$$

*The boundary data is described by*

$$\begin{aligned}
\mathbf{v}_f(t) = \bar{\mathbf{v}}^{in}(t) \quad & on\ \Gamma_f^{in}, \\
\rho_f v_f \mathbf{n} \cdot \nabla \mathbf{v}_f - p\mathbf{n} = 0 \quad & on\ \Gamma_f^{out}, \\
\mathbf{u}_s = 0 \quad & on\ \Gamma_s,
\end{aligned} \tag{10.13}$$

*where $\mathbf{n}$ is the outward facing normal vector and $\bar{\mathbf{v}}^{in}$ is an averaged inflow profile that depends on the width of the blood vessel.*

## 10.3   Monolithic Schemes for the Coupled Problem

In this section, we derive monolithic variational formulations for Problem 10.1 in ALE and in *Fully Eulerian* coordinates. Growth can lead to substantial deformations of the solid up to a full closure of the vessel. Together with the stiff coupling between blood and tissue, this is a prototypical application for the Eulerian framework introduced in Chap. 6.

**Problem 10.2 (Long-Scale Problem in ALE Formulation)**   *Find the fluid velocity* $\hat{\mathbf{v}}_f \in \bar{\mathbf{v}}^{in}(t) + \mathcal{V}_f$, *deformation* $\hat{\mathbf{u}} \in \mathcal{W}$ *and the pressure* $\hat{p}_f \in \mathcal{L}_f$, *such that*

$$\left(\hat{\rho}_f \hat{J}_f \hat{\mathbf{v}}_f \cdot \hat{\mathbf{F}}_f^{-1} \hat{\nabla} \hat{\mathbf{v}}_f, \hat{\phi}_f\right)_{\hat{\mathcal{F}}} + \left(\hat{J}_f \hat{\sigma}_f \hat{\mathbf{F}}^{-T}, \hat{\nabla} \hat{\phi}\right)_{\hat{\mathcal{F}}} + \left(\hat{\mathbf{F}} \hat{\boldsymbol{\Sigma}}, \hat{\nabla} \hat{\phi}\right)_{\hat{\mathcal{S}}} = 0 \quad \forall \hat{\phi} \in \mathcal{W},$$

$$\left(\widehat{\operatorname{div}}\left(\hat{J} \hat{\mathbf{F}}^{-1} \hat{\mathbf{v}}_f\right), \hat{\xi}_f\right)_{\hat{\mathcal{F}}} = 0 \quad \forall \hat{\xi} \in \mathcal{L}_f,$$

*with* $\boldsymbol{\Sigma}$ *as given in (10.6) and where the extension* $\hat{\mathbf{u}}_f$ *is defined as*

$$\left(\hat{\nabla} \hat{\mathbf{u}}_f, \hat{\nabla} \hat{\psi}_f\right)_{\hat{\mathcal{F}}} = 0 \quad \forall \hat{\psi}_f \in \mathcal{W}_f,$$

*in the case of the harmonic extension. For the biharmonic extension we use*

$$\left(\hat{\mathbf{w}}_f, \hat{\chi}_f\right)_{\hat{\mathcal{F}}} - \left(\hat{\nabla} \mathbf{u}_f, \hat{\nabla} \hat{\chi}_f\right)_{\hat{\mathcal{F}}} + \left(\hat{\nabla} \hat{\mathbf{w}}_f, \hat{\nabla} \hat{\psi}_f\right)_{\hat{\mathcal{F}}} = 0 \quad \forall \{\hat{\psi}_f, \hat{\chi}_f\} \in \tilde{\mathcal{W}}_f \times \mathcal{W}_f$$

*The elastic deformation gradient is defined in (10.4) depending on the concentration of foam cells. The latter one is defined by the ode*

$$\partial_t c_s^* = \gamma(\boldsymbol{\sigma}_{WS}, t), \quad c_s^*(0) = 0.$$

*The function spaces are given by*

$$\mathcal{V}_f = [H_0^1(\hat{\mathcal{F}}; \hat{\mathcal{I}} \cup \hat{\Gamma}_f^{in})]^2, \qquad \mathcal{L}_f = L^2(\hat{\mathcal{F}}),$$

$$\mathcal{W} = [H_0^1(\hat{\Omega}; \hat{\Gamma}_f^{in} \cup \hat{\Gamma}_s)]^2, \quad \mathcal{W}_f = [H_0^1(\hat{\mathcal{F}})]^2, \quad \tilde{\mathcal{W}}_f = [H^1(\hat{\mathcal{F}})]^2.$$

*Remark 10.3 (Biharmonic Mesh Model)* We have chosen a mixed formulation for the biharmonic extension, such that an efficient discretization with simple $C^0$-conforming finite elements is possible.

To express the coupled model including growth in *Fully Eulerian* coordinates, we must carry over the decomposition of the deformation gradients into the current system. We denote the inverse mappings of $\hat{T}_a$ and $\hat{T}_e$ by $T_a = \hat{T}_a^{-1}$ and $T_e = \hat{T}_e^{-1}$ and their gradients by $F_a = \nabla T_a$ and $F_e = \nabla T_e$ respectively. Using $\mathbf{F} = \hat{\mathbf{F}}^{-1}$, we have

$$\mathbf{F} = \hat{\mathbf{F}}^{-1} = \hat{\mathbf{F}}_a^{-1} \hat{\mathbf{F}}_e^{-1} =: \mathbf{F}_a \mathbf{F}_e. \tag{10.14}$$

Although a direct modeling in Eulerian coordinates is possible, we derive the Eulerian solid model by a mapping of the Lagrangian formulation to the Eulerian system

$$J_s\hat{\rho}_s^0(\partial_t\mathbf{v}_s + \mathbf{v}_s \cdot \nabla\mathbf{v}_s) - \text{div}\left(J\mathbf{\Sigma}\mathbf{F}^{-T}\right) = 0$$
$$\partial_t\mathbf{u}_s + \mathbf{v}_s \cdot \nabla\mathbf{u}_s = \mathbf{v}_s \qquad \text{in } \mathcal{S}(t), \tag{10.15}$$

where $\mathbf{\Sigma}$ is given in (10.6) with an Eulerian description

$$\mathbf{\Sigma} = J_a^{-1}\mathbf{F}_a\mathbf{\Sigma}_e\mathbf{F}_a^T,$$
$$\mathbf{\Sigma}_e = 2\mu\mathbf{E}_e + \lambda_s\,\text{tr}(\mathbf{E}_e)I, \quad \mathbf{E}_e = \frac{1}{2}(\mathbf{F}_e^{-T}\mathbf{F}_e^{-1} - I). \tag{10.16}$$

Frei [151] gives details on the transformation of the stresses of an active material to the Eulerian coordinate framework.

### 10.3.1   Solid Growth in Eulerian Coordinates

Next, we carry over the growth model to the Eulerian representation. We will use again the simple isotropic growth model

$$\hat{\mathbf{F}}_a = \hat{g}I \tag{10.17}$$

and define the Eulerian growth function $g$ by setting $g(x, t) = \hat{g}(\hat{x}, t)$. By the relation $\mathbf{F}_a = \mathbf{F}_a^{-1}$, it holds that

$$\mathbf{F}_a = g^{-1}I. \tag{10.18}$$

By the decomposition (10.14) it follows that

$$\mathbf{F}_e = \mathbf{F}_a^{-1}\mathbf{F} = g\mathbf{F}, \quad J_e = g^2 J_s. \tag{10.19}$$

The complete Eulerian stresses are given by

$$J_a\sigma_e\mathbf{F}_a^{-T} = J_s\mathbf{F}_e^{-1}\mathbf{\Sigma}_e\mathbf{F}^{-T} = g^{-1}J_s\mathbf{F}^{-1}(2\mu_s\mathbf{E}_e + \lambda_s\,\text{tr}(\mathbf{E}_e)I)\mathbf{F}^{-T}, \tag{10.20}$$

with the Eulerian elastic strain tensor

$$\mathbf{E}_e = \frac{1}{2}(g^{-2}\mathbf{F}^{-T}\mathbf{F}^{-1} - I). \tag{10.21}$$

Finally, we derive the equation of mass conservation in Eulerian coordinates. We assume that homogenous material with the same parameters is added, such that the

density is constant $\hat{\rho}_a = \hat{\rho}_s$. Hence, if $m(\hat{V})$ is the mass of the reference state, $m(\hat{V}_a)$ is the mass of the grown material, which is conserved in the current configuration $V$

$$m(\hat{V}) = \int_{\hat{V}} \hat{\rho}_s^0 \, d\hat{x}, \quad m(\hat{V}_a) = \int_{\hat{V}_a} \hat{\rho}_a \, d\hat{x}^g = \hat{\rho}_s^0 \int_{\hat{V}} \hat{J}_a \, d\hat{x} = \hat{\rho}_s^0 \int_V \hat{J}_a J_s \, dx,$$

(10.22)

where $\hat{J}_a := \det(\hat{\mathbf{F}}_a) = \hat{g}^2$ is the determinant of the growth part, such that for the density $\rho$ of the current configuration it holds

$$\rho = \hat{\rho} = g^2 \hat{\rho}_s^0 J_s.$$

(10.23)

**Problem 10.4 (Long-Scale Problem in Fully Eulerian Coordinates)**   *Find velocity* $\mathbf{v}_f(t) \in \bar{\mathbf{v}}^{in} + \mathcal{V}_f$, *deformation* $\mathbf{u} \in \mathcal{W}$ *and pressure* $p_f \in \mathcal{L}_f$, *such that*

$$\left( \rho_f \mathbf{v}_f \cdot \nabla \mathbf{v}_f, \phi_f \right)_{\mathcal{F}(t)} + \left( \sigma_f, \nabla \phi \right)_{\mathcal{F}(t)} + \left( J_a \sigma_e \mathbf{F}_a^{-T}, \nabla \phi \right)_{\mathcal{S}(t)} = 0 \quad \forall \phi \in \mathcal{W}$$

$$\left( \operatorname{div} \mathbf{v}_f, \xi_f \right)_{\mathcal{F}(t)} = 0 \quad \forall \xi_f \in \mathcal{L}_f,$$

$$\left( \nabla \mathbf{u}_f, \nabla \psi_f \right)_{\mathcal{F}(t)} = 0 \quad \forall \psi_f \in \mathcal{W}_f.$$

*The elastic deformation gradient is defined in (10.19). Accumulation of foam cells is described by the ode*

$$\partial_t c_s^* = \gamma(\sigma_{WS}, t).$$

*The function spaces are defined as*

$$\mathcal{V}_f = H_0^1(\mathcal{F}(t); \mathcal{I}(t) \cup \Gamma_f^{in})^2, \qquad \mathcal{L}_f = L^2(\mathcal{F}(t)),$$
$$\mathcal{W} = H_0^1(\Omega(t); \Gamma_f^{in} \cup \Gamma_s)^2, \qquad \mathcal{W}_f = H_0^1(\mathcal{F}(t))^2.$$

## 10.4   Numerical Tests

Studying different test cases we compare the performance of two different formulations of the fluid-structure interaction problem, the *Arbitrary Lagrangian Eulerian* formulation from Chap. 5 and the *Fully Eulerian* formulation detailed in Chap. 6. We give further tests and an elaborate discussion in [158].

### 10.4.1   Problem Setting

As geometry we use a channel with length 10 cm and an initial width $\omega(0)$ (of the fluid part) of 2 cm as illustrated in Fig. 10.3. The solid parts on the top and

bottom have an initial thickness of 1 cm each. Fluid density and viscosity are given by $\rho_f = 1\,\mathrm{g \cdot cm^{-3}}$ and $\nu_f = 0.3\,\mathrm{cm^2 \cdot s^{-1}}$. The solid parameters are given by $\rho_s = 1\,\mathrm{g \cdot cm^{-3}}$ and the Lamé parameters $\nu_s = 10^4$ and $\lambda_s = 4 \cdot 10^4\,\mathrm{dyn \cdot cm^{-2}}$. We prescribe a pulsating velocity inflow profile on $\Gamma_f^{\mathrm{in}}$ given by

$$\mathbf{v}^{\mathrm{in}}(t, x, y) = \frac{3}{2} \begin{pmatrix} \mathbf{v}^{\mathrm{in}}(t)(1 - y^2) \\ 0 \end{pmatrix},$$

$$\mathbf{v}^{\mathrm{in}}(t) = \left( \varepsilon_\omega + 5\omega(t) \right)(1 + \sin(2\pi t))\mathrm{cm \cdot s^{-1}}, \tag{10.24}$$

depending on the width of the channel $\omega(t)$ (see Fig. 10.3). The parameter $\varepsilon_\omega$ is used to control the minimum flow rate and will be specified below. These parameters are similar to a real plaque growth configuration. The remaining boundary conditions are specified in (10.13). For the growth, we specify a function that depends on the concentration of the foam cells $c_s^*$ that is defined by the ode (10.11). Growth is centered around the middle part of the vessel

$$\hat{g}(\hat{x}, \hat{y}, t) = 1 + c_s^*(t)\exp\left(-\hat{x}^2\right)(2 - |\hat{y}|), \quad \hat{\mathbf{F}}_g(\hat{x}, \hat{y}, t) := \hat{g}(\hat{x}, \hat{y}, t)\,I. \tag{10.25}$$

Growth $\hat{g}$ and inflow rate $\mathbf{v}^{\mathrm{in}}(t)$ implicitly depend on the solution. As the configuration is symmetric in the vertical direction, we consider the lower half of the geometry for the simulation only.

The problem is driven by a parabolic inflow profile with an average inflow rate $\bar{\mathbf{v}}^{\mathrm{in}}(t)$. We use the averaged inflow profile of (10.24)

$$\bar{\mathbf{v}}^{\mathrm{in}}(t) = \left( \varepsilon_\omega + 5\omega(t) \right)\mathrm{cm \cdot s^{-1}} \tag{10.26}$$

The dynamic configuration using the pulsating inflow field (10.24) is discussed in [158]. We discretize the coupled problem by a splitting in time and approximate by the following iteration.

**Definition 10.5 (Mechano-Chemical Iteration)**  Initialize $\mathbf{v}^0 = 0$, $\mathbf{u}^0 = 0$, $g^0 = 0$ and the vessel-width $\omega^0 = 2$. Set time step $k_l = 0.1\,\mathrm{days} = 8\,640\,\mathrm{s}$. Iterate for $n = 1, 2, \ldots$.

1.          Solve (10.1)        $\{c_s^{*,n-1}, \omega^{n-1}\} \mapsto \{\mathbf{v}^n, \mathbf{u}^n, p^n\}$

2.    Compute wall stress        $\boldsymbol{\sigma}_{WS}^n = \displaystyle\int_{\mathcal{I}} |\boldsymbol{\sigma}_f(\mathbf{v}^n, p^n)\mathbf{n} \cdot \mathbf{e}_1|\,do$

3.        Update foam cells        $c_s^{*,n} = c_s^{*,n-1} + k_l\gamma_0\left(1 + \boldsymbol{\sigma}_{WS}^n/\bar{\boldsymbol{\sigma}}\right)^{-1}$

4.   Compute vessel width        $\omega^n = 2 - 2\mathbf{u}_2^n(A(t_n), t_n)$

First, we choose a minimum inflow velocity of $\varepsilon_\omega = 0.1\,\mathrm{cm/s}$. In Fig. 10.4, the streamlines of the fluid and the deformed vessel walls at times $t = 10\,\mathrm{days}$ and $t = 50\,\mathrm{days}$ are shown.
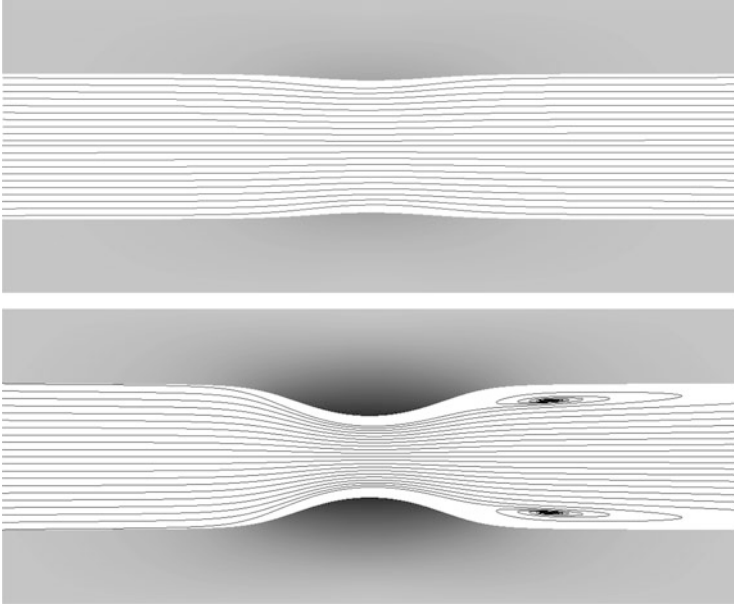
**Fig. 10.4** Solution after 10 days (*top*) and 50 days (*bottom*). Streamlines of the fluid and the deformation of the vessel wall are shown

In Fig. 10.5 we show the course of different output functionals over time: the wall stress in main stream direction on the vessel wall $\mathcal{I}$ that is computed in step 2. of the iteration, the channel width $\omega(t) = 2 - 2\mathbf{u}_2(A(t_n))$ in the middle point $A(t_n)$ (see Fig. 10.3), the vorticity of the solution in the $L^2$-norm and the outflow at the right boundary defined by

$$J_{\text{vort}}(\mathbf{v}) = \int_{\mathcal{F}(t)} \left( \partial_y \mathbf{v}_1 - \partial_x \mathbf{v}_2 \right)^2 \, dx, \quad J_{\text{out}}(\mathbf{v}) = \int_{\Gamma_{f,\text{out}}} \mathbf{v} \cdot \mathbf{n}. \qquad (10.27)$$

The functional values for the *Arbitrary Lagrangian Eulerian* method (harmonic and biharmonic extension) and the *Fully Eulerian* approach show very good agreement. Using the harmonic extension, the ALE method broke down at $t = 63.2$ days due to degeneration of mesh cells, with the biharmonic extension, we were able to get results up to $t = 109.3$ days.

The fully Eulerian method, on the other hand, was able to yield reliable results until the channel was almost closed. As the inflow velocity is bounded from below by $\varepsilon_\omega = 0.1 \, \text{cm} \cdot \text{s}^{-1}$ and as the fluid is incompressible, a passage must always remain. As higher wall stresses slow down plaque growth, see (10.11), the vertical displacement approaches a limit. However, increasing fluid-dynamical forces cause strong horizontal deflections that finally result in a breakdown of the simulation.
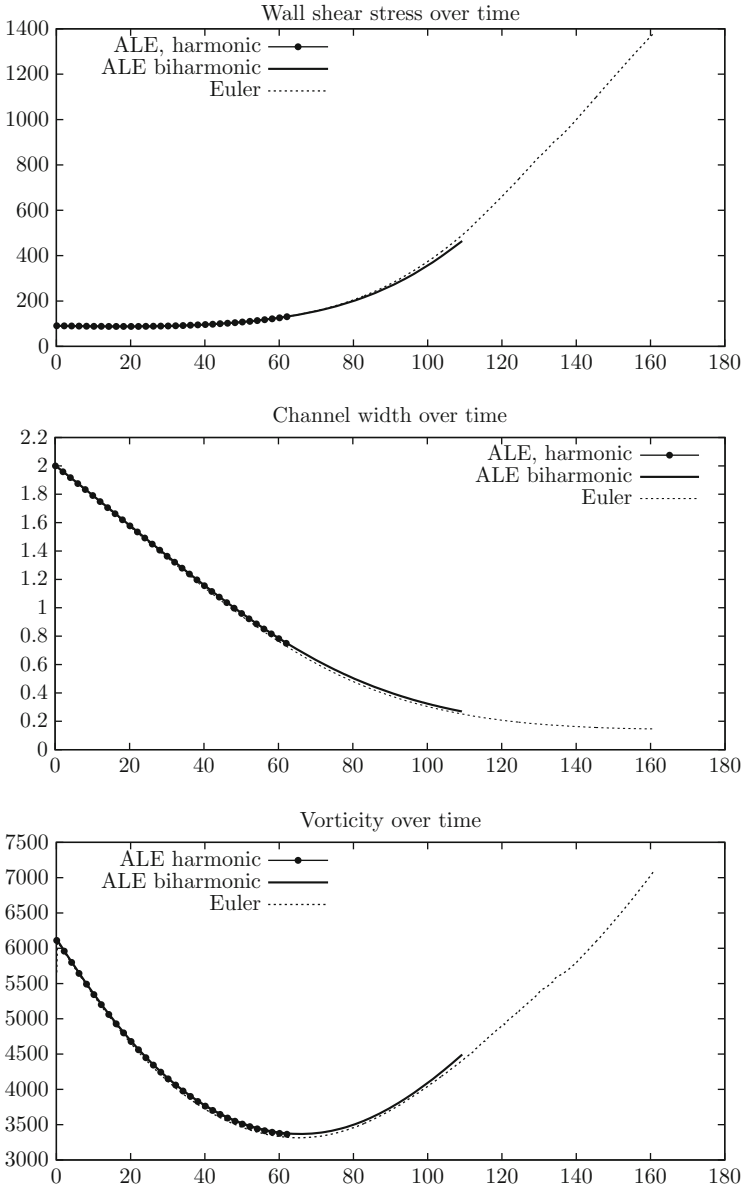
**Fig. 10.5** Course of different output functionals over time during closing of channel. For small deformations, the three different modeling approaches give similar results. Once the deformation gets larger, the two ALE approaches with harmonic and biharmonic extensions will fail

As the results for the ALE method with harmonic and biharmonic extension are nearly identical until time $t = 63.1$ days, we will not show the harmonic variant anymore in the following tests.

In Fig. 10.6, we present the deformed meshes at time $t = 109.3$ days for the ALE approach with biharmonic mesh deformation and the fully Eulerian approach. In the case of the biharmonic ALE approach, this was the last mesh before the calculation broke down.

Next, we study the convergence with respect to the spatial grid size $h > 0$ for both the fully Eulerian and the ALE technique. The results are shown in Table 10.1. For the fully Eulerian approach, we use $Q^1 - Q^1$ equal-order elements and meshes with 256, 1024 and 4096 patch elements. For the ALE approach we use $Q^2 - P^{1,\text{dc}}$ elements as introduced in Sect. 4.3.1. We choose slightly coarser meshes for a fair comparison.
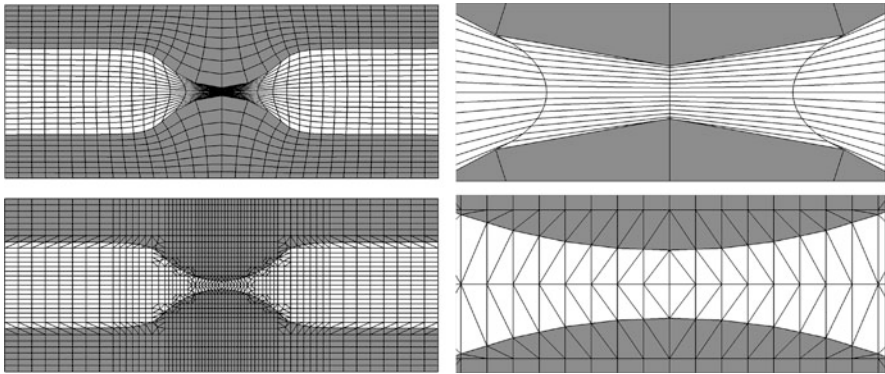


**Fig. 10.6** *Top*: Biharmonic deformation close to breakdown at $t = 109.3$ days and zoom-in (*right*). *Bottom*: Corresponding results using the *Fully Eulerian* approach on fixed meshes

**Table 10.1** Convergence of functional values at $t = 50$ days on three different grids for the fully Eulerian and the ALE approach

| #patches | Wall stress | Width | Vorticity | Outflow |
|---|---|---|---|---|
| Euler 256 | $1.033 \cdot 10^2$ | 1.092 | $3.408 \cdot 10^3$ | 9.251 |
| 1024 | $1.050 \cdot 10^2$ | 1.064 | $3.457 \cdot 10^3$ | 9.547 |
| 4096 | $1.060 \cdot 10^2$ | 1.052 | $3.472 \cdot 10^3$ | 9.648 |
| Extrapol. | $1.074 \cdot 10^2$ | 1.047 | $3.479 \cdot 10^3$ | 9.700 |
| Conv. | 0.77 | 1.81 | 1.71 | 1.55 |
| ALE 160 | $1.087 \cdot 10^2$ | 1.033 | $3.527 \cdot 10^3$ | 9.892 |
| 640 | $1.076 \cdot 10^2$ | 1.037 | $3.515 \cdot 10^3$ | 9.849 |
| 2560 | $1.073 \cdot 10^2$ | 1.038 | $3.510 \cdot 10^3$ | 9.834 |
| Extrapol. | $1.072 \cdot 10^2$ | 1.039 | $3.506 \cdot 10^3$ | 9.826 |
| Conv. | 1.87 | 1.49 | 1.26 | 1.52 |

We indicate estimated convergence rates and extrapolated limits

   We evaluate the functionals at $t = 50$ days. The functional values for the ALE and the fully Eulerian approach converge roughly against the same values. Small differences are due to time discretization (the time step has been chosen as 0.1 days). Further, the implementation of the *Fully Eulerian* model is only semi-implicit, as the domain layout during the time step $t_n \rightarrow t_{n+1}$ is fixed to $\mathcal{F}^n$ and $\mathcal{S}^n$.

   Furthermore, we estimated the convergence order for all functionals, see Table 10.1. Besides the wall stress, all estimated convergence orders lie between linear and quadratic convergence order and the ALE and the fully Eulerian approach converge similarly. The ALE approach, however, seems to yield better values already on very coarse grids. Furthermore, the ALE approach shows faster convergence in the wall stress functional. The reason for this better performance is the use of inf-sup stable $Q^2$ elements in the case of ALE, which is not yet possible with the parametric interface approximation scheme described in Sect. 4.5, where stabilized $Q^1 - Q^1$ elements are utilized.

   An interesting aspect from a modeling point of view is the question if the channel closes completely or if there will remain a small layer of fluid between the vessel walls. As discussed before, a complete closure of the channel is not possible as long as the inflow rate $\varepsilon_\omega$ is positive.

   To study closure, we decrease the minimal inflow velocity $\varepsilon_\omega$ from 0.1 to 0 and the velocity inflow by a factor of 10 to

$$\mathbf{v}_1^{\text{in}} = 0.15 \cdot (5\omega(t))(1 - y^2) \, \text{cm/s}. \tag{10.28}$$

This means that the flow through the narrow part of the channel will decrease considerably when the channel is almost closed. This has two important effects: First, the fluid forces acting against the growth of the solid are much smaller. Secondly, the wall stress becomes smaller which has a strengthening impact on the solid growth in our model. Altogether, this has the effect that in our simulation the channel closes completely at time $t = 55.8$ days. Of course full closure is only possible by using the *Fully Eulerian* formulation.

   In Fig. 10.7, we show plots of the channel width and the vorticity over time. In contrast to the larger inflow velocity studied above, the fluid forces (e.g. the vorticity) decrease after $t \approx 40$ days which makes the closure of the channel possible. In Fig. 10.8, we show the last mesh obtained with the fully Eulerian approach ($t = 55.8$ days) where the channel is completely closed. The ALE calculation (with biharmonic extension) broke down at time $t = 40.6$ days.

   These simplified simulations consider an averaged inflow velocity only. The main mechanical forcing however is due to the pulsating blood flow. In [158] a two-scale approach has been suggested, where effective parameters for the wall stress are computed from isolated short-scale simulations that resolve the pulsation. It is shown that substantial variations in plaque growth up to 20% exist.
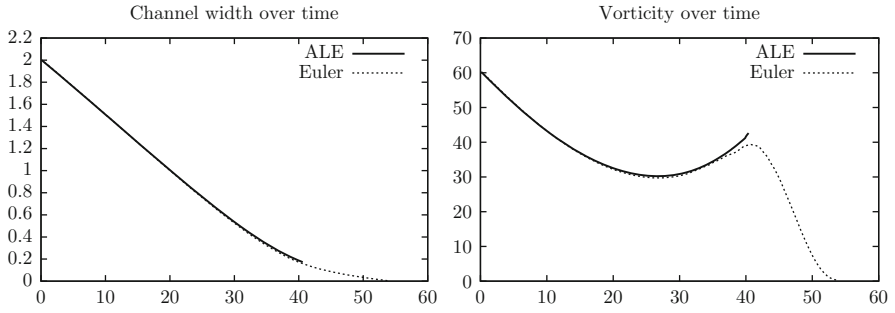
**Fig. 10.7** Channel width and vorticity for a long-scale simulation with reduced inflow velocity. The inflow velocity goes to zero when the channel closes. This makes the complete closure of the channel possible
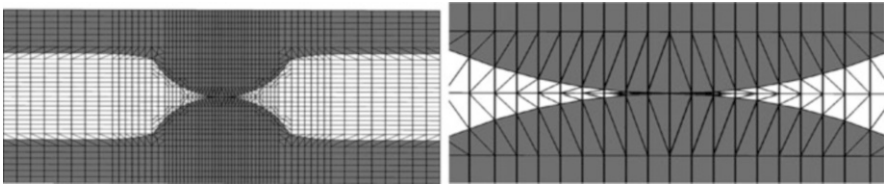


**Fig. 10.8** Second test case. *Fully Eulerian* deformation at complete closure $t = 55.8$ days